



Science Arts & Métiers (SAM)

is an open access repository that collects the work of Arts et Métiers Institute of Technology researchers and makes it freely available over the web where possible.

This is an author-deposited version published in: <https://sam.ensam.eu>
Handle ID: <http://hdl.handle.net/10985/25641>

To cite this version :


Guillaume NORDET, Cyril GORNY, Frédéric COSTE, Pierre LAPOUGE, Albin EFFERNELLI, Etienne BLANCHET, Patrice PEYRE - Influence of laser wavelength on the powder bed fusion of pure copper - Progress in Additive Manufacturing - 2024

Any correspondence concerning this service should be sent to the repository

Administrator : scienceouverte@ensam.eu



Influence of laser wavelength on the powder bed fusion of pure copper

Guillaume Nordet^{1,2}  · Cyril Gorny¹ · Frédéric Coste¹ · Pierre Lapouge¹ · Albin Effernelli² · Etienne Blanchet² · Patrice Peyre¹

Abstract

In the current work, and for the first time, two 1 kW continuous wave (CW) lasers, with green and infrared (IR) wavelengths, were used to manufacture pure copper with the laser powder bed fusion (LPBF) process. Copper is among the most complex materials to build with LPBF because of its high conductivity and high reflectance under IR irradiation, preventing easy densification. Various aspects were investigated: (1) the stability domain of single LPBF tracks vs (laser power, scan speed) conditions, (2) the porosity rate of 3D samples, (3) the induced microstructures, and (4) the electrical properties of as-built and heat-treated samples. Densification levels of more than 99.5% could be obtained either with an IR Gaussian laser or with green top-hat laser irradiation, but with a wider process parameter window for the green conditions, and higher productivity. The obtained as-built microstructures were mostly columnar and oriented toward the build direction, with a $\langle 110 \rangle$ main texture. The as-built copper also exhibits a $\sim 10^{15} \text{ m}^{-2}$ dislocation density determined through the X-ray diffraction peak broadening analysis. Finally, up to 95% IACS (international annealed copper standard) electrical conductivities were measured on LPBF test specimens. Such results provide new and useful information on choosing an adequate laser wavelength to optimize the LPBF process on pure copper.

Keywords Green · IR · Laser · Copper · Powder bed fusion · Microstructures · X-ray

1 Introduction

Laser powder bed fusion (LPBF) additive manufacturing is now recognized as one of the most innovative technologies for designing and building complex geometric shapes.

The physics of the laser–powder–melt pool interaction has been studied for at least 5 years using dedicated diagnostics such as high-speed imaging. Such diagnostics are installed on many homemade laboratory set ups like Bidare et al.’s work [1], or large-scale facilities such as time-resolved X-ray radiography on a synchrotron (Zhao et al. [2]) which allow probing the fused matter at a high resolution.

A large range of materials can be manufactured with LPBF. Pure copper is a crucial material for electrical or

heat-exchanger applications [3]. Still, it remains a complex material to build with LPBF, due to the combination of high reflectance under IR irradiation ($\sim 95\%$) and high thermal conductivity ($390 \text{ W}\cdot\text{m}^{-1}\cdot\text{K}^{-1}$). This promotes a low laser–material energy coupling, and limits powder consolidation compared with usual LPBF materials (stainless, steels, nickel-based alloys, titanium alloys). In recent years, a systematic investigation of LPBF copper manufacturing with IR lasers has been made by authors like Jadhav et al. [4, 5] and Colopi et al. [6]. Their first publications showed that 98.5% was the maximum densification that could be reached on pure copper using IR irradiation. They also have indicated that the use of higher power lasers ($> 700 \text{ W}$) than those available on classical LPBF machines was a key point to densify copper but could induce damages in optics as indicated by Jadhav et al. in [4]. A more recent work by the same authors [5] has shown that it was possible to densify copper up to 99.3% with a 500 W IR laser and $800 \text{ mm}\cdot\text{s}^{-1}$ scan speed, due to the use of a small laser diameter of $37.5 \mu\text{m}$ at $1/e^2$, favoring the formation of a keyhole regime. On the other

✉ Guillaume Nordet
guillaume.nordet@ensam.eu

¹ PIMM Laboratory, Arts et Métiers Institute of Technology, CNRS, CNAM, HESAM University, 151 Bd de l’Hôpital, 75013 Paris, France

² AddUp, 5 Rue Bleue, 63118 Cebazat, France

hand, Colopi et al. [6], using a 600 W–1 kW IR laser with a 78 μm laser diameter, demonstrated the benefit of multi-pass re-melting to obtain nearly fully dense copper with up to 99% density, and with large scan speeds of more than 1000 mm/s allowing build rates of 2.6 cm^3/h . From these studies, one can conclude that a satisfactory LPBF manufacturing of copper is possible, with IR laser but due to adaptations of the process. Another recent study on pure copper by Yan et al. [7] demonstrated a satisfactory densification level up to 99.1% with surprisingly much lower laser powers (250 W and 400 W) and a 100 μm laser diameter. The thin powder layers used in this study (30 μm) could partially explain how such a result could be obtained. However, for such low power levels, microstructures exhibit a lack of fusion and unmelted powders.

Two main solutions have been tested and reported in the literature to improve the laser–copper energy coupling.

The first one is to functionalize the copper powder surface to improve its absorptance. For instance, Jadhav et al. [8] have shown that a 100 nm oxide layer obtained by heat treatment allowed obtaining similar copper density (98%) for a 40% lower energy density due to a factor two increase of the powder bed absorptance (from 0.32 to 0.58). The same authors [9] obtained a similar benefit with using carbon particles incrustated on top of the copper particles, but a strong reduction of mechanical resistance and electrical conductivities ($\sim 39\%$ IACS) mainly due to carbon and oxygen segregation. Nickel and tin coatings, provoking an equivalent factor two increase of the powder bed absorptance, were also tested successfully by Lindstrom et al. [10] with a benefit on densification rate but electrical conductivity has not been measured.

However, densification levels remained much lower ($< 99.5\%$) than those achievable with the electron powder bed fusion technique ($> 99.9\%$), as shown in a recent work by Thomas et al. [11]. With a nearly similar approach, Jadhav et al. [12] obtained a 99.6% density on a 0.3% Sn-coated copper powder using a 500 W IR laser and a 600 $\text{mm}\cdot\text{s}^{-1}$ scan speed. However, due to the alloying effect of Sn, a reduced electrical conductivity (80% IACS, international annealed copper standard) was obtained, compared with pure copper.

Last, Hu et al. [13] have also satisfactorily used Y_2O_3 particles on CuCrZr alloys to improve the laser absorptance and refine LPBF microstructures.

The second possible solution to improve LPBF applied to copper is to use recently developed green or blue lasers to improve the copper absorptance. Green lasers have already been validated for copper welding for a long time, as shown by Engler et al. in 2011 [14], and applied recently to the case of gap welding by Chung et al. [15]. Punzel et al. [16] also demonstrated that both the IR and green laser welding

processes could be stabilized by wobbling, but that the green laser process was more stable in terms of spatter generation and surface aspect.

Moreover, Nordet et al. [17] have shown that with a green laser irradiance, the absorptance at a liquid state during LPBF tracks could be increased by a factor of 2 compared with similar IR tests, which is comparatively lower compared with the absorptance gap at a solid state (4% for an IR wavelength and 40% for a green source). Such a result reduces the benefit of green wavelengths over IR wavelengths in LPBF, as the laser is mostly absorbed on a liquid layer.

Kohl et al. [18] have also reported that the sudden change of IR absorption from solid to liquid state (4% to 12%) led to unstable processing and spatters. In contrast, with a green wavelength, more stable processing conditions are obtained due to the smoother absorptance transition from solid to liquid state (40–22%).

Blue high-power diode lasers, operating at 450 nm, have also been tested successfully for copper welding by Hummel et al. [19] due to the overall absorptance of the blue wavelength. However, blue laser diodes currently for sale are still limited in terms of brightness, especially for LPBF applications requiring high scanning speeds and small laser diameters. Finally, even if an industrial LPBF machine operating with an 800 W green laser has been for sale recently [20], no parametric investigation of copper powder bed manufacturing with a green laser has been published up to now.

Therefore, the comparison of IR and green LPBF is the main objective of the current experimental work carried out on the same LPBF chamber with two 1 kW CW lasers: an IR source ($\lambda = 1080$ nm) and a green source ($\lambda = 515$ nm) having nearly similar laser spot diameters at the focal position.

The global objectives were to analyze: (1) the densification rate for IR or green process conditions, (2) the induced microstructures, including an estimation of dislocation density, and (3) the electrical conductivity of as-built and heat-treated LPBF samples, to provide a comprehensive contribution to the LPBF of copper with various wavelengths.

2 Experimental conditions

2.1 LPBF tests

Green laser trials were performed using a commercial 1 kW CW green laser TruDisk 1020 from Trumpf^{GmbH} already used in [21], operating at 515 nm. The 168 mm focus lens allowed obtaining a 90 μm top-hat beam at a focal distance.

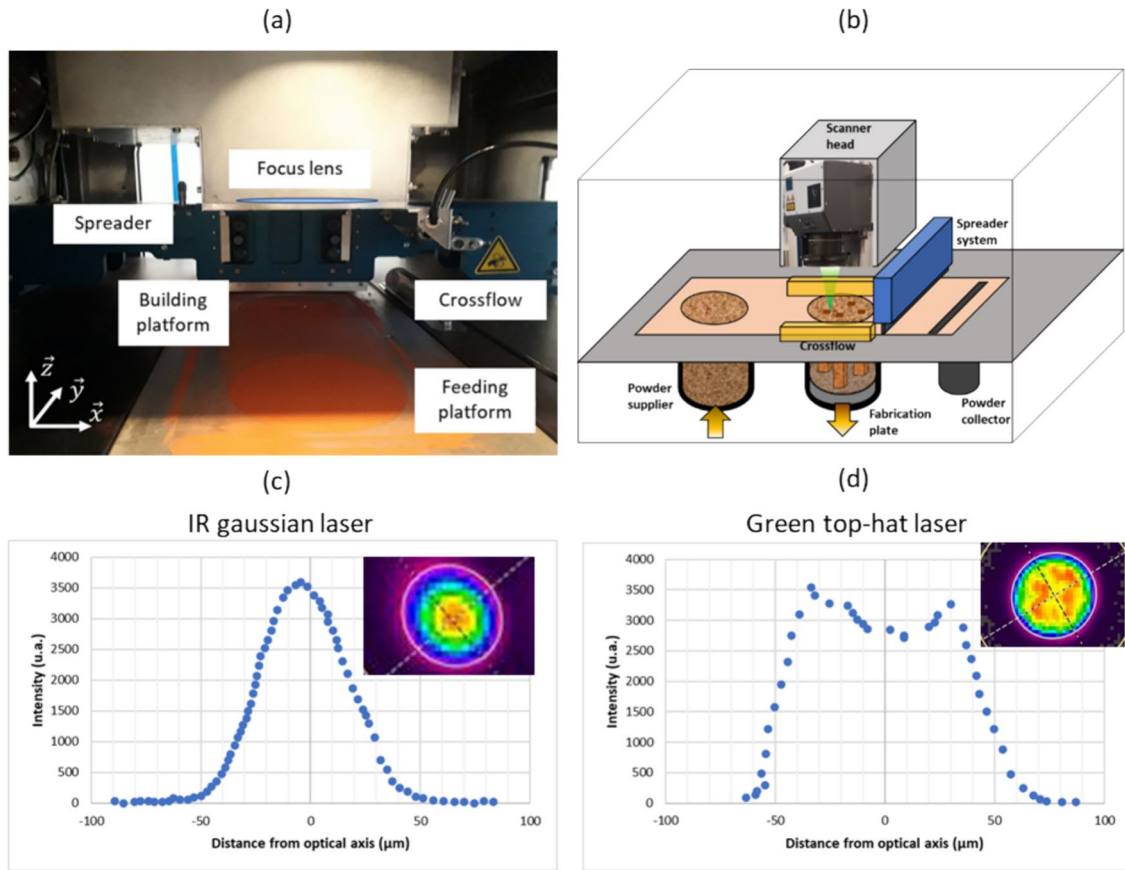


Fig. 1 Laser beam distributions: **a** opened LPPBF setup, **b** schematic illustration, **c** IR laser (Gaussian, 70 μm diameter), **d** green laser (top-hat, 90 μm diameter)

Near-infrared LPPBF tests were carried out with a 1 kW RedCube SPI laser at a 1080 nm wavelength and a 400 mm focus lens to achieve a 60–80 μm (at $1/e^2$) Gaussian laser beam. A large chamber LPPBF setup (Fig. 1a), already detailed in recent work by Sow et al. [20], was used to implement the two lasers and carry out single beads and 3D cubic or parallelepiped samples, with Argon shielding and oxygen rate of fewer than 500 ppm.

Table 1 summarizes the operating parameters of the two lasers used in the current study: the maximum power (P_{max}) of the lasers, the spot diameter at the focal point, their shape, and the scan speed range (V).

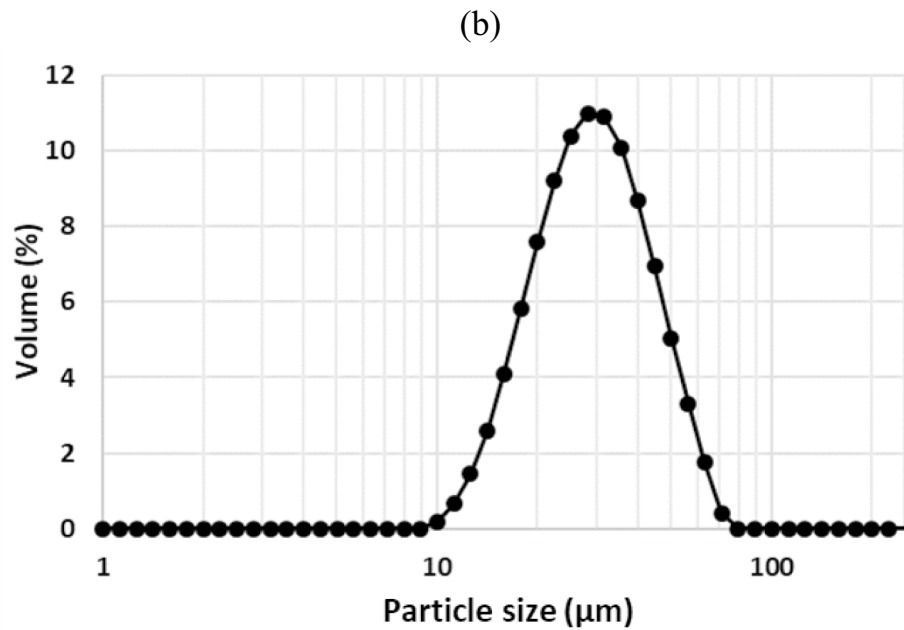
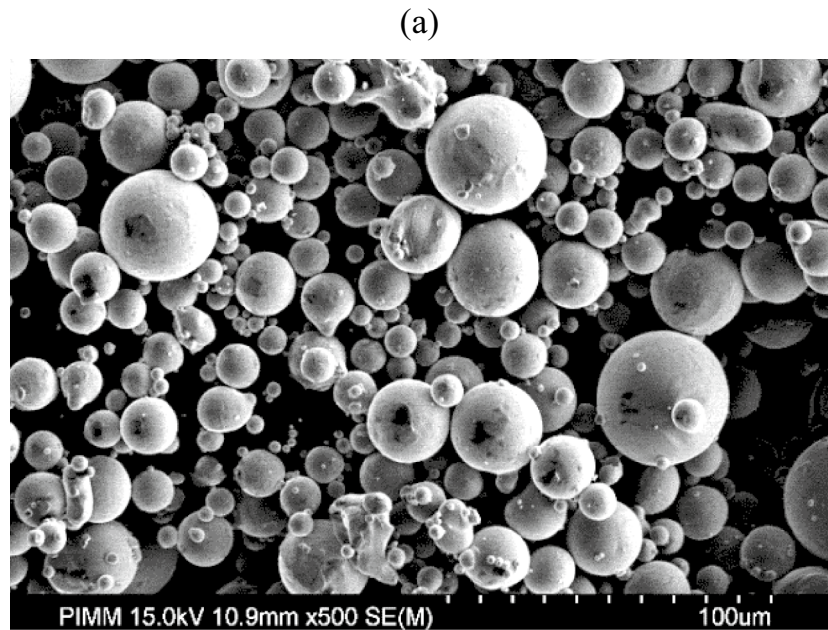
A gas-atomized copper powder with a 15–45- μm size distribution was used (Fig. 2). The powder was dried at 60 $^\circ\text{C}$ in a UF 110 Memmert drying oven for at least 24 h

before testing to favor spreading. This controlled drying stage was shown to modify the powder color to some extent but with a moderate effect on the powder bed absorptance. The drying stage was used to improve spreading conditions, and favor powder flowability. However, no specific rheological analysis of the powder before and after drying was carried out. A polymer spreader deposited the 60- μm to 150- μm -thick powder layers on the building plateau. The building plate was a 316L steel base plate. For all 3D cubic or parallelepiped samples, a 1-mm-height support grid was built between the sample and the build plate.

Table 1 LPPBF conditions with IR and green wavelengths

λ	P_{max} (W)	Spot diameter (μm)	Shape	V range (m/s)	Laser
1.08 μm	1000	70	Gaussian	0.3–0.8	RedCube 1 kW SPI
0.515 μm	1000	90	Top-hat	0.2–1	TruDisk 1020

Fig. 2 Gas-atomized pure copper powder (15–45 μm range). **a** SEM image, **b** powder distribution



2.2 Microstructural analysis

For microstructural analysis, samples were cut, mounted in an epoxy resin, and polished with SiC papers (up to the 4000 grade), and with 3 μm , 1 μm diamond suspensions, and OPS (colloidal silica) final polishing. For the specific preparation of EBSD surfaces, samples were demounted

and electropolished with a D2 electrolyte using a *Struers Lectropol 5* system, and 18 V–20 s etching conditions.

A 1/3 chlorhydric acid – 2/3 acetic acid + saturation with picric acid chemical etching was used for optical microscopy observations. Two techniques were used for estimating materials' density: metallographic examination before chemical etching combined with image analysis (using ImageJ software), and Archimedes double weighing technique (in air and ethanol). EBSD analysis was carried out on an *EVO MA-40 Zeiss SEM*, equipped with a Nordif

UF-1000 camera. Inverse pole figures (IPF) were obtained using the *OIM DC Nordif* software.

X-ray diffraction tests mostly focused on analyzing peak broadening and 2nd–3rd order residual stresses, were carried out using a Cu anticathode ($\lambda = 0.154$ nm) and an XPERT PANalytical θ – 2θ goniometer.

2.3 Methodology

First, (P, V) stability diagrams have been obtained over a large power sweep speed range to determine the P–V operating conditions allowing the creation of continuous mono-beads for each wavelength. This bead stability study is used in the sequel to determine preferential laser scanning conditions.

For the IR laser tests carried out at PIMM Lab., the LPBF setup (Fig. 1) is the same as presented by Sow et al. [20]. Following preliminary investigations indicating that dense copper could not be obtained with powers below 800 W, two measurement sets were carried out at 1000 W power and 500 mm/s speed, 200 μ m hatching, and a 60 μ m layer height. As a defocusing of the laser beam was supposed to occur during long continuous tracks, a pause time of 100 ms was imposed between each bead to cool down the optics and reduce the defocusing effect.

The first set of parts (IR 1–6) allows the size variation of the parts (from 5×5 mm² to 21×21 mm² surface). Parts had the same 5-mm height (83 layers) and the same scan strategy: stripes consisting of a line scanning with anti-parallel stripes and a 200 μ m hatch and a 90° or (for only 1 sample) 67° rotation between each layer (Table 2).

The second set of pieces (IR 7–12) shows the feasibility of obtaining dense pieces ($15 \times 15 \times 5$ mm³) by changing the scanning strategy. Three different scanning strategies have been tested, detailed in Table 2

- In (IR-7–8–9), we have tested the influence of a chess strategy: with different chess sizes (5×5 mm² or 3×3 mm² square), and a change in rotation angle (90° or 67° hatch rotation).
- (IR-10) was built with the same stripe strategy and rotation angle as IR-5.
- (IR-11–12) were also performed using a stripe strategy, with a 75- μ m slice applied between each layer to reduce overlap.

Finally, the AddUp company has built 3D parts using the optimized scanning conditions on its own LPBF setup to confirm preliminary tests at PIMM Lab.

The 1 kW green laser and its scan head were installed on the same LPBF setup (Fig. 1) as previously used in Ref. [20] but with a much shorter focus distance of 170 mm. A 90° rotation angle between layers and a stripes scan strategy were systematically used. All samples were 15-mm cubic samples. Three powder layer heights were considered: 60 μ m, 100 μ m, and 150 μ m address the potential benefits of a green wavelength on build rates. Power (400–1000 W), speed (0.2–1 m/s), and hatch (100–300 μ m) values are reported in Tables 3 and 4 with porosity rate results for each sample.

For these tests, the densities of the parts have been measured on a metallographic cross-section after cutting—polishing (down to OPS silica suspension) of the parts. Images are then captured with an optical microscope at $\times 100$ magnification. By binarizing these images, the porosity rate can be determined by counting the black pixels and comparing them to the total number of pixels. The error bars were estimated by making 3–5 cuts on each sample.

A last set of trials was carried out to measure the electrical conductivity of parts depending on the

Table 2 LPBF conditions with an IR wavelength ($\lambda = 1080$ nm), $D = 70$ μ m, Gaussian influence of scan strategy and sample dimension (hatch distance $H = 200$ μ m and layer thickness $\Delta h = 60$ μ m for all conditions)

Sample	P (W)	V (m/s)	VED (J/mm ³)	Size (mm \times mm)	Building strategy	Porosity (%)
IR-1	1000	0.5	520	5 \times 5	Stripes: 90° angle	0.3
IR-2	1000	0.5	520	7.5 \times 7.5	Stripes: 90° angle	0.2
IR-3	1000	0.5	520	10 \times 10	Stripes: 90° angle	2.25
IR-4	1000	0.5	520	15 \times 15	Stripes: 67° angle	3.5
IR-5	1000	0.5	520	15 \times 15	Stripes: 90° angle	5.6
IR-6	1000	0.5	520	21 \times 21	Stripes: 90° angle	17
IR-7	1000	0.5	520	15 \times 15	Chess: 5 mm \times 5 mm 90° angle	0.55
IR-8	1000	0.5	520	15 \times 15	Chess: 3 mm \times 3 mm 90° angle	0.67
IR-9	1000	0.5	520	15 \times 15	Chess: 5 mm \times 5 mm 67° angle	0.73
IR-10	1000	0.5	520	15 \times 15	Stripes: 90° angle	4.1
IR-11	1000	0.5	520	15 \times 15	Stripes: 90° angle with a slice	6.4
IR-12	1000	0.5	520	15 \times 15	Stripes: 67° angle with slice	4.55

Table 3 LPBF conditions with a green wavelength ($\lambda = 515$ nm)–15 mm cubic samples ($D = 90$ μm , top-hat, $\Delta h = 60$ μm layer height)

Name	h (μm)	P (W)	V (m/s)	VED (J/mm^3)	EBV (J/mm^3)	Density	Porosity rate
G-1	120	300	0.4	117.9	104.2	95.52%	4.48%
G-2	120	400	0.4	157.2	138.9	98.09%	1.91%
G-3	120	500	0.4	196.5	173.6	98.53%	1.47%
G-4	120	600	0.4	235.8	208.3	99.20%	0.80%
G-5	120	700	0.4	275.1	243.1	99.83%	0.17%
G-6	120	800	0.4	314.4	277.8	99.78%	0.22%
G-7	120	900	0.4	353.7	312.5	99.45%	0.55%
G-8	120	1000	0.4	393.0	347.2	99.68%	0.32%
G-9	100	700	0.4	275.1	291.7	99.30%	0.70%
G-10	120	300	0.5	94.3	83.3	93.59%	6.41%
G-11	120	400	0.5	125.8	111.1	95.76%	4.24%
G-12	120	500	0.5	157.2	138.9	98.35%	1.65%
G-13	120	600	0.5	188.6	166.7	99.75%	0.25%
G-14	120	700	0.5	220.1	194.4	99.84%	0.16%
G-15	120	800	0.5	251.5	222.2	99.70%	0.30%
G-16	100	400	0.5	125.8	133.3	96.55%	3.45%
G-17	100	500	0.5	157.2	166.7	96.18%	3.82%
G-18	100	500	0.6	131.0	138.9	95.73%	4.27%
G-19	100	700	0.6	183.4	194.4	98.38%	1.62%
G-20	100	700	0.3	366.8	388.9	99.83%	0.17%
G-21	100	700	0.8	137.5	145.8	92.54%	7.30%
G-22	100	600	0.8	117.9	125.0	92.55%	7.45%

Table 4 LPBF conditions with a green wavelength ($\lambda = 515$ nm)–15 mm cubic samples ($D = 90$ μm , top-hat, $\Delta h = 100$ and 150 μm layer heights)

Name	Δh (μm)	Hatch H (μm)	P (W)	V (mm/s)	VED (J/mm^3)	Porosity rate	Build rate (cm^3/h)
G-24	100	300	1000	400	393	0.70%	43.2
G-25	100	300	1000	500	314	0.63%	54
G-26	100	150	1000	800	196	3.12%	43.2
G-27	100	150	800	500	252	1.35%	27
G-28	100	150	800	600	210	2.68%	32.4
G-29	100	125	500	500	157	5.94%	22.5
G-30	100	125	400	400	157	3.89%	18
G-31	100	125	600	500	189	5.02%	22.5
G-32	100	125	700	700	157	1.79%	31.5
G-33	100	250	700	400	275	0.12%	36
G-34	100	250	800	400	314	0.2%	36
G-35	100	150	1000	700	225	1.8%	37.8
G-36	150	300	1000	400	393	0.37%	64.8
G-37	150	300	1000	500	314	1.16%	81
G-38	150	150	1000	800	196	0.57%	64.8
G-39	150	150	800	500	252	1.6%	40.5
G-40	150	125	800	600	210	1.4%	48.6
G-41	150	125	500	500	157	8.4%	33.75
G-42	150	125	500	500	189	5.5%	27
G-43	150	125	400	400	157	6.9%	18

porosity rate. Parts are not cubic but $25 \times 10 \times 5$ mm parallelepipeds. For those parts, each face has been handily polished and measured. Density was measured with a single weighing after checking the real volume of the built parts.

3 Stability diagrams on single fusion tracks

Using (P = laser power, V = scan speed) stability diagrams is a well-known, yet an insufficient method for providing a preliminary set of optimum process conditions for a given powder layer thickness. The objective is to carry out single LPBF tracks and checking, with a simple surface analysis,

the (P , V) stability domains where neither balling nor humping effects are dominant.

These trials were conducted using both IR and green laser irradiations. Powder layers of approximately $100 \mu\text{m}$ were manually spread on a copper substrate, corresponding to a layer height of roughly $50 \mu\text{m}$ due to the $\sim 50\%$ compactness of the powder bed.

(P , V) diagrams are shown in Fig. 3 for IR irradiation and Fig. 4 for green irradiation. The first aspect to notice is that “continuous” LPBF tracks on pure copper are less linear and stable than on usual LPBF alloys (Fe, Ti, or Ni based), since they always exhibit an oscillating shape (tracks number 3 in Fig. 3a and b). This traduces limited wetting and local destabilizations of the melt pool by the surrounding powder bed. This phenomenon can be due to the low surface

Fig. 3 a (P , V) stability diagrams for single LPBF tracks at the IR wavelength, b top view and cross-section for (1) 500W–0.5 m/s, (2) 750W–0.5 m/s, and (3) 1000W–0.5 m/s

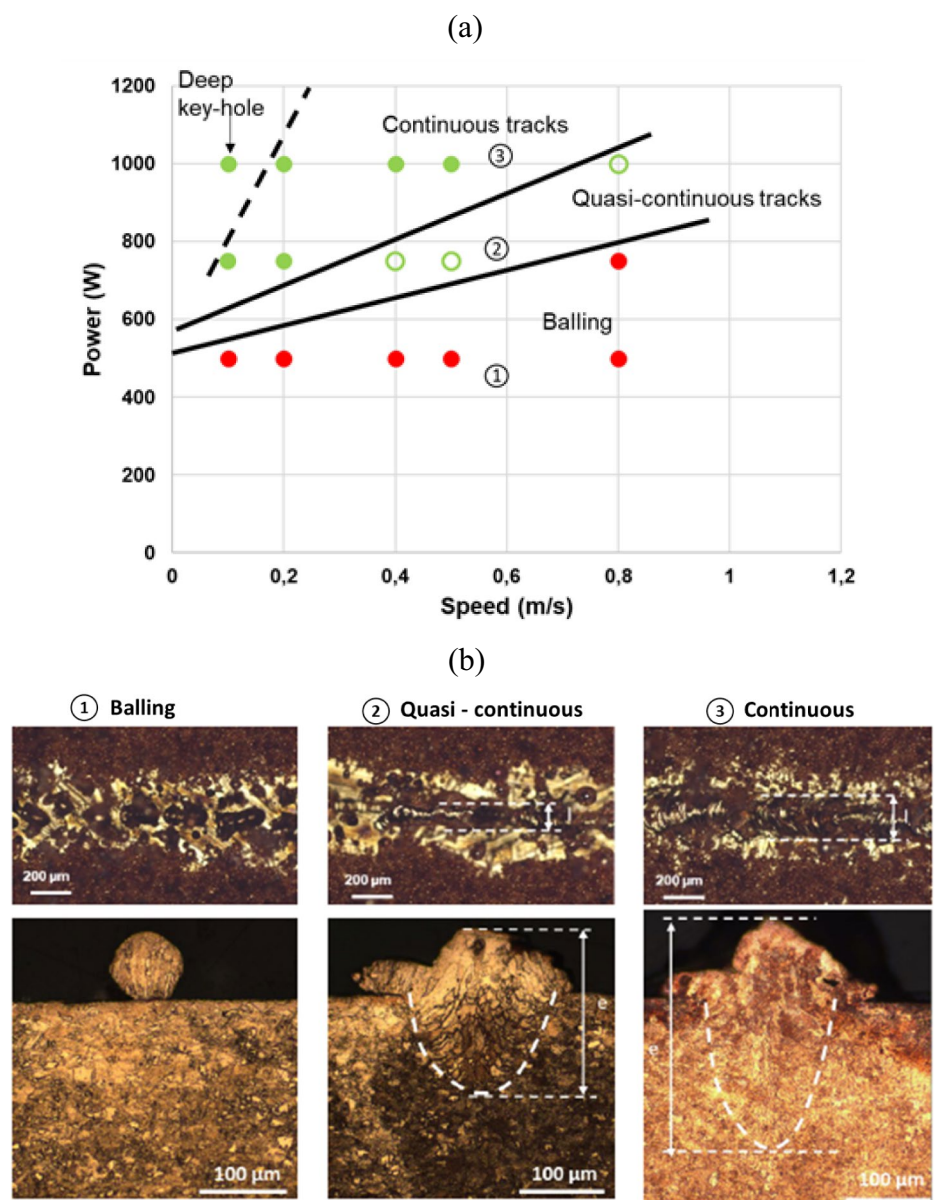
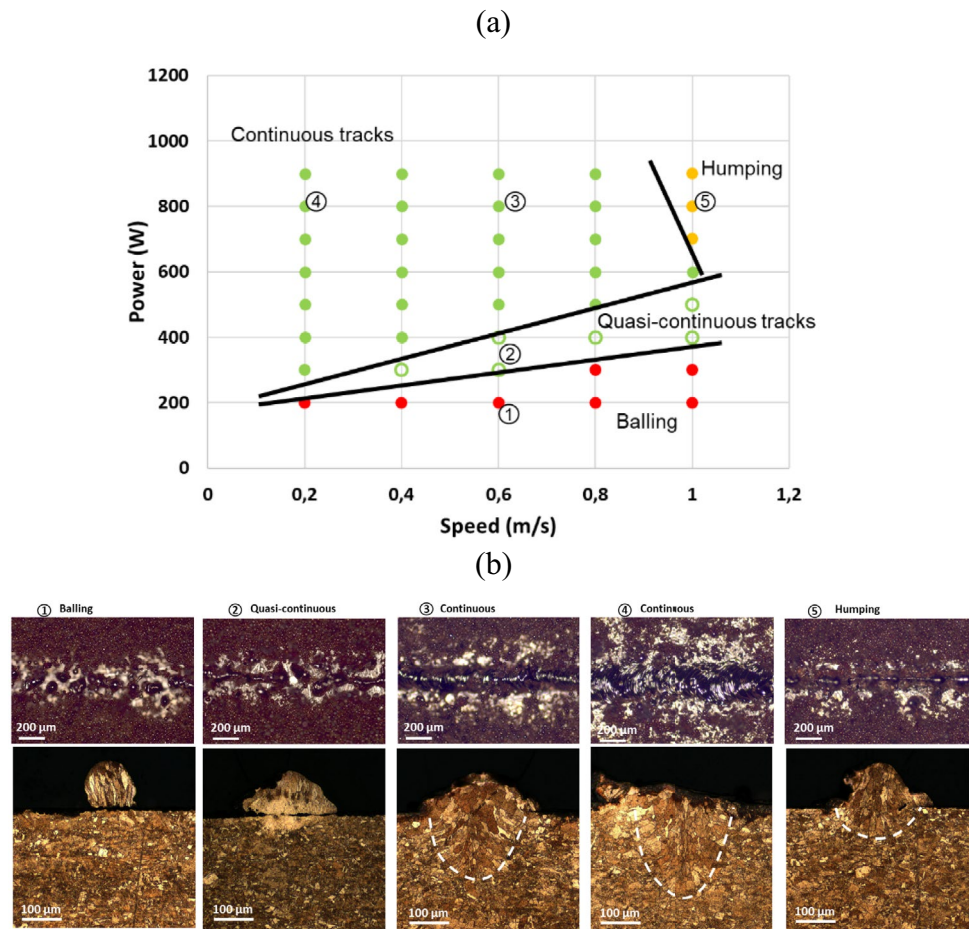


Fig. 4 a (P, V) stability diagrams for single LPBF tracks at the green wavelength, **b** top view for (1) 200 W–0.6 m/s, (2) 300 W–0.6 m/s, (3) 800 W–0.6 m/s, (4) 800 W–0.2 m/s, (5) 800 W–1 m/s



tensions of liquid copper ($\gamma = 1.2 \text{ N/m}$) [22] that favor the melt pool/gas interface destabilization.

More globally, results indicate a much smaller stable regime in IR than in green, with only four stable scan speeds at 1000 W: 0.1, 0.2, 0.4, and 0.5 m/s, and two at 800 W: 0.1 and 0.2 m/s for $\lambda = 1080 \text{ nm}$. Cross-sections and top view analyses carried out for the continuous tracks, number 3 in Fig. 3, at 1000 W–0.5 m/s have shown a width of 230 μm and a depth of 400 μm .

For $\lambda = 515 \text{ nm}$, stable LPBF tracks are obtained for much lower powers, mostly above 400 W. A brief comparison of these two diagrams (IR vs green) also indicates roughly a factor 2 decrease of the laser power stability threshold at a given scan speed with a green wavelength: from 700 to 300 W at 0.2 m/s and 1000–500 W at 0.8 m/s. As an example of a continuous track, at 800 W–0.6 m/s (number 3 in Fig. 4) has shown a width of 230 μm and a depth of 400 μm .

Considering that laser absorption mostly occurs on a melt pool surface, this result is in full agreement with the two times higher absorptance of liquid copper A_{Liq} at 515 nm, 23.5% vs 11% at 1080 nm (IR) [14, 17].

Such results suggest that similar stable process windows would be achieved with green and IR LPBF if we consider

the absorbed power at the melt pool surface $A_{\text{Liq}} P$ in a ($A_{\text{Liq}} P, V$) representation.

Due to the small process window evidenced on 100- μm -thick powder layer at 1080 nm, the 3D process optimization will be restricted to the 800–1000 W range for IR wavelength and 400–1000 W range for the green irradiation in the next parts of the paper.

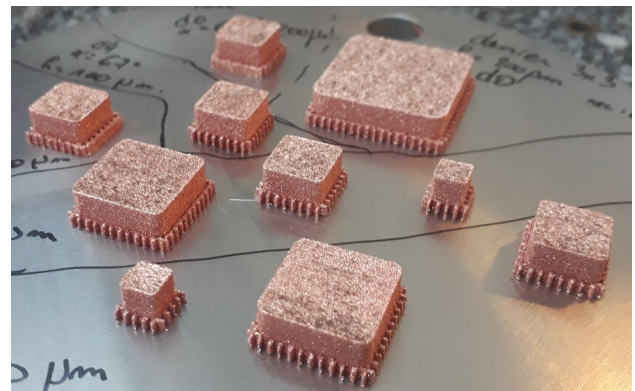


Fig. 5 LPBF samples obtained with a 1.08 μm near-IR wavelength (without contouring)

4 LPBF manufacturing of 3D parts

4.1 Experimental method: LPBF of copper with a 1.08 μm (IR) and green (0.515 μm) wavelengths

Preliminary LPBF tests were made on PIMM facilities using a 1 kW near-infrared (IR) fiber laser, to optimize densification rate. Different parallelepiped samples, having different build sections, were considered (Fig. 5), with a zigzag stripe strategy for hatching, and without contours. In this configuration, the average length of laser vectors depends linearly on the build section edge: between 5 mm \times 5 mm, and 21 mm \times 21 mm.

Experimental conditions are reported in Table 2, including the volume energy density VED calculated with Eq. 1 here below. Such a VED value, defined as the ratio between laser powder density (W/m^2) and scan speed (m/s), was selected as a significant parameter of the process, following analytical welding models by Fabbro [23] who defined a linear dependency of normalized molten depth with such a VED formulation.

$$\text{VED} = \frac{4P}{V\pi D^2}, \quad (1)$$

where P =laser power, V =scan speed, D =laser diameter.

On the results presented in Fig. 6, a unique (P , V) condition of (1000 W, 0.5 m/s) was used, with a 200 μm hatch distance and a $\Delta h = 60 \mu\text{m}$ layer height. Using a

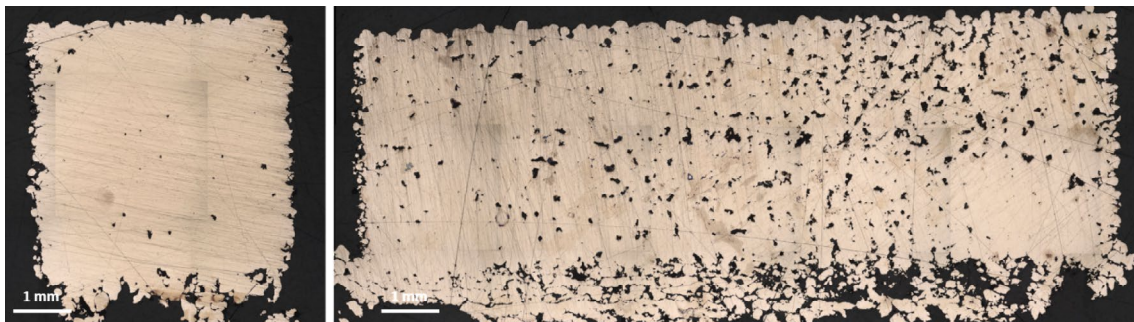
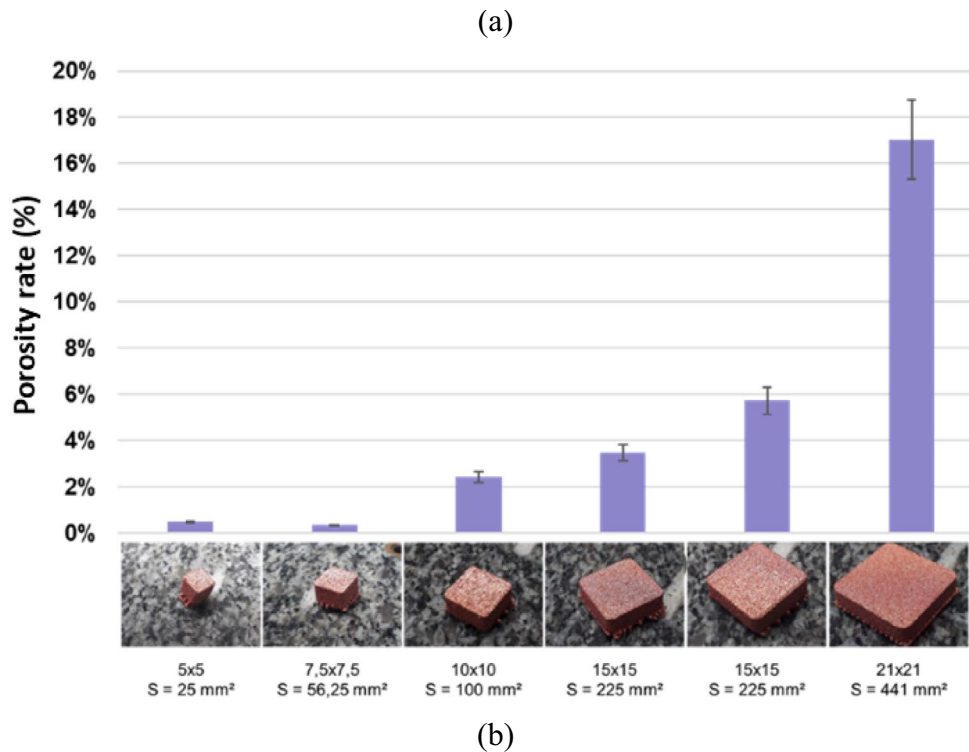


Fig. 6 **a** Porosity vs sample size for similar process conditions, **b** cross-sections for a 5 mm \times 5 mm sample (0.3% porosity) and a 15 mm \times 15 mm sample (5% porosity)

single hatch distance for IR trials (Table 2) is a rather unusual choice compared to process optimization on classical materials (steels, titanium nickel-based). However, preliminary investigations have shown that using a lower hatch distance than 200 μm was not a satisfactory means for improving densification on pure copper because in that case, the laser was fully positioned in the denudated zone, which induced a limited absorptance and a loss of fusion.

Surprisingly, results (IR-1 to IR-6) clearly show an increase of porosity with build area: from 0.3% for small samples, and up to 17% for the larger ones. Two explanations are then possible:

1. For excessive vector length ΔX_{laser} corresponding to longer lasting times $\Delta t_{\text{laser}} = \Delta X_{\text{laser}}/V$, a thermally induced modification of non-cooled optics at high power can occur as indicated in Ref. [3], resulting in a defocusing of the laser beam. In the presented example, such an effect is expected to occur above $0.0075/0.5 = 0.015$ s lasing time.
2. A more classical size effect: reducing the length of the laser track promotes local preheating from the track n to the track $(n + 1)$, due to a reduced cooling time. This could enlarge fusion tracks and favor densification. However, in the configuration used, a 0.1-s pause was imposed between each track to prevent excessive heating of the optics. An additional cooling time is expected to limit local preheating effects at the melt pool scale. For this reason, the most probable explanation is a laser defocusing at 1 kW, promoted by unstable optics. Anyway, this confirms that a porosity of less than 0.5% can be obtained on pure copper with a near-IR wavelength, and a Gaussian laser beam diameter around 70 μm .

A second set of experiments, which used a modified scan strategy, confirmed this effect. In that case, using a chess strategy, with chess dimensions of (3 mm \times 3 mm) or (5 mm \times 5 mm), allowed for obtaining satisfactory densification, around 0.7% porosity, on 15 mm \times 15 mm \times 5 mm parallelepipeds. On the same sample size, a stripe strategy, with a 67° or 90° between subsequent layers, generated 4% to 6.5% porosity (Fig. 7).

To prevent hindering laser defocusing effects, a final set of LPBF trials was made at ADDUP LPBF research center, with a similar 1 kW fiber laser, but more stable optics at high laser power. The results obtained were fully satisfactory, with up to 99.8% densification of the built material, provided laser powers exceeded 800 W. Such densification levels are higher than those presented already in the literature with similar [3, 5] or lower [4] IR laser powers. They were obtained with a deep keyhole LPBF mode, corresponding to

melt pool depths between 200 and 300 μm (Fig. 9), and melt pool aspect ratio (depth e /spot diameter D) of 3–4. Finally, it was concluded that copper densities superior to 99.5% could be obtained with a near-IR laser with a ~ 80 μm spot diameter and 60 μm layer heights, but only for powers above 800 W. An indicative build rate (Eq. 2) is near 21 cm^3/h for the LPBF conditions used in Fig. 8, which is 50% higher than fusion rates obtained by Colopi et al. [6] (Fig. 9).

$$\text{Build rate} = V * \Delta h * H \quad (2)$$

4.2 LPBF of copper with a 0.515- μm wavelength

Table 3 presents all LPBF conditions used with the green laser and the porosity rates obtained for those parts. All parts are 15-mm cubic samples built with the same 60- μm layer height.

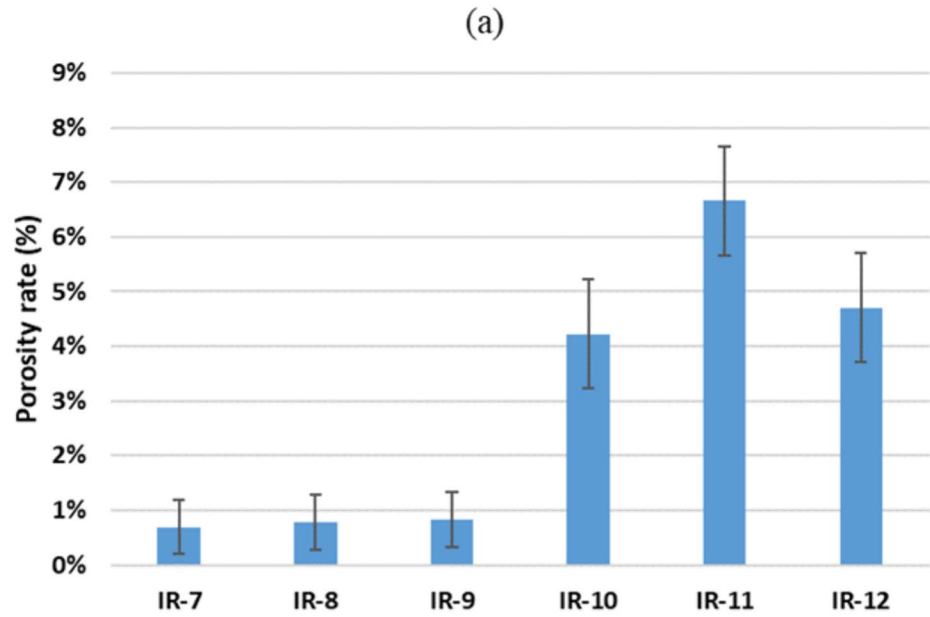
For a constant layer height of $\Delta h = 60$ μm and a hatch distance of 100–120 μm (Table 3), the following conclusions were made from the observed data in terms of porosity rates:

- Maximum densification rates are near 99.9%. They are obtained for scan speeds = 0.4–0.5 m/s, and laser powers superior to 600 W (Fig. 10b). Such maximum densification levels are 0.1–0.3% better than those obtained in IR.
- Beyond 0.5–0.6 m/s, regardless of the laser power and hatch distance, porosity increases. For instance, at 1000 $\text{mm}\cdot\text{s}^{-1}$, the porosity rate is systematically above 0.5% (Fig. 11a and b).
- Such data suggest a scan speed threshold around 500 $\text{mm}\cdot\text{s}^{-1}$ above which fusion tracks are more unstable and increase porosity.
- An estimation of porosity rate vs scan speed is seen in Fig. 12, for laser powers between 500 and 900 W. Optimum densifications are obtained for VED values above 200 J/mm^3 (to be compared with ~ 50 –70 J/mm^3 for a 316L steel) and the porosity vs VED curve roughly follows a $1/\text{VED}^2$ dependence (Fig. 12)

Even if these results were obtained with a nearly constant hatch distance, they confirm a scan speed limit of around 500 $\text{mm}\cdot\text{s}^{-1}$. The minimum porosity rate is near 0.8%.

A second set of trials was carried out with deeper manufacturing layers of 100 μm and 150 μm heights (Table 4). Corresponding results (porosity vs VED) are shown in Fig. 13. They confirm the ability of a green laser source to provide porosity levels of less than 1% with both 100 μm and 150 μm layer heights, for high VED values (> 300 J/mm^3) and maximum laser power (1 kW) corresponding to a deep keyhole regime ($e > 200$ μm). Interestingly, this allows obtaining a satisfactory

Fig. 7 Influence of scan strategy on porosity on 15 mm×15 mm×5 mm samples estimated with metallography technique: **a** porosity rate vs scan strategy (experimental data correspond to samples IR-8 and IR-10 in Table 2), **b** for a 5 mm×5 mm chess strategy (0.7% porosity), **c** for a stripe strategy and a 90° rotation angle (L90): 4.2% porosity



(b)



(c)



densification level (~99.5%) combined with elevated build rates (Eq. 2) up to 64 cm³/h for $\Delta h = 150 \mu\text{m}$, $P = 1000 \text{ W}$ – hatch $H = 300 \mu\text{m}$, $V = 400 \text{ mm}\cdot\text{s}^{-1}$. This result provides an interesting insight into the ability of a 1 kW green wavelength to manufacture dense copper with elevated fusion rates.

4.3 Microstructures

The microstructural analysis on both (O, x, y) and (O, x, z) planes, (with O = origin of the coordinate system, and x, y, z directions), reveals a columnar microstructure oriented toward the build direction (BD), with the occurrence of

Fig. 8 Influence of IR laser power on porosity rate (10 mm × 10 mm × 10 mm samples): **a** 800 W–0.5 m/s (99.7% average density), **b** 1000 W–0.5 m/s (99.6% average density) ($H=200\ \mu\text{m}$, $\Delta h=60\ \mu\text{m}$)

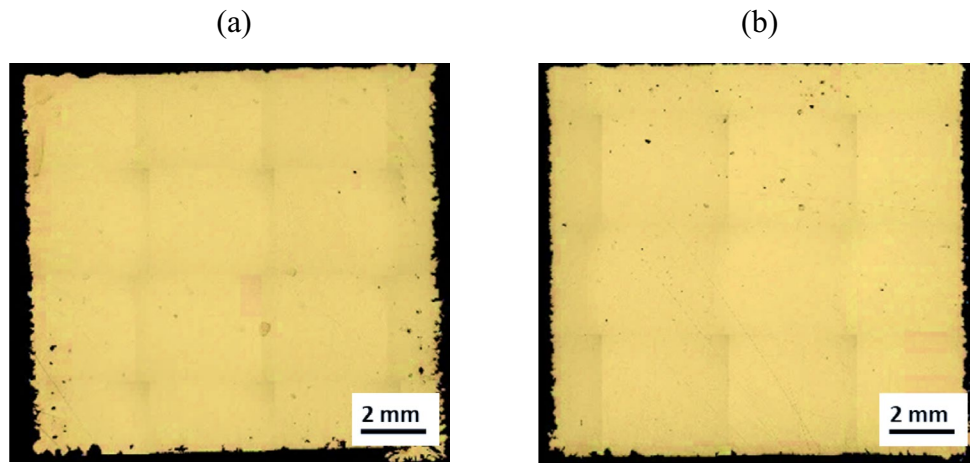


Fig. 9 Observation of solidified melt pools at the last build layer (800 W–0.5 m/s). As Cu is a pure metal, fusion zones of approximately 200–220- μm depth are only detectable with the grain orientations

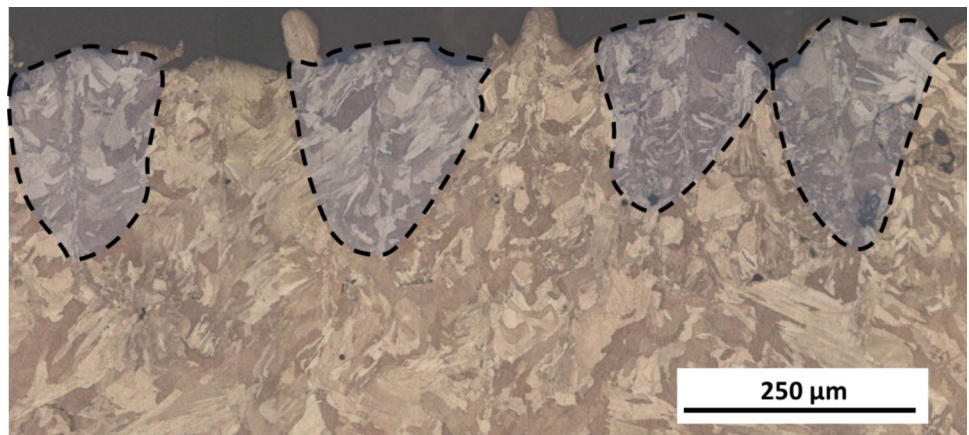
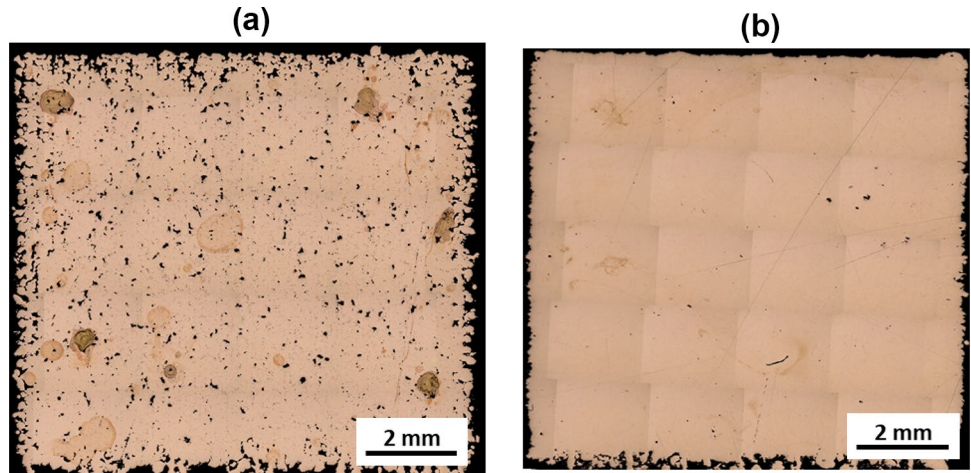


Fig. 10 LPBF cubic samples manufactured with the green laser at 0.5 m/s scan speed ($\Delta h=60\ \mu\text{m}$) with **a** 300 W (G-10 sample) and **b** 500 W laser power (G-12 sample) and hatch distance = 120 μm



chevrons located at the center of large vertical columns (Fig. 14a). Due to the 90° angle, columns exhibit a squared shape on the (O, x, y) plane, with scanning lines perpendicular to each other (Fig. 14a). On (O, x, z) cross-sections, the microstructure appears surprisingly clearer after OPS polishing, and without chemical etching

(Fig. 14b). One can distinguish the continuous columnar growth aligned with the melt pool root of each two layers for the 90° rotation angle strategy (zone ①). Within large parallelepiped columns, chevrons are formed due to lateral epitaxy between adjacent melt pools (at zone ②).

Fig. 11 LPBF cubic samples manufactured with the green laser at $1000 \text{ mm}\cdot\text{s}^{-1}$ with **a** 600 W, **b** 800 W laser power, hatch distance = $120 \mu\text{m}$

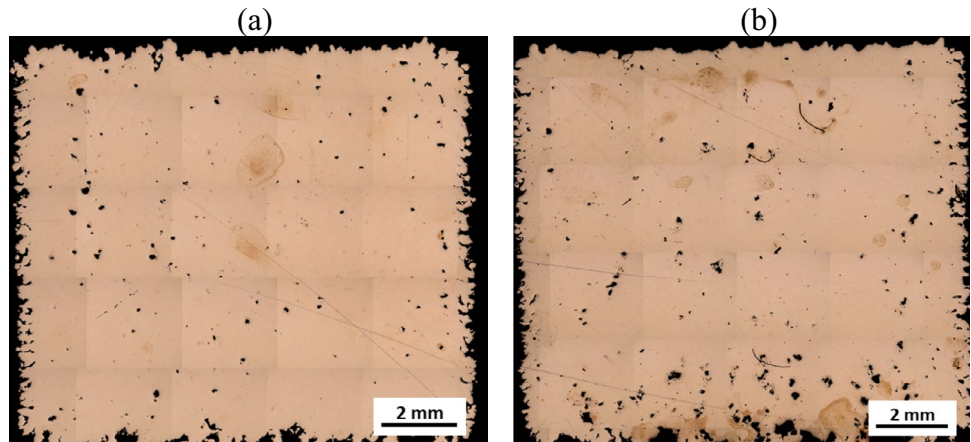


Fig. 12 Porosity vs VED ($\Delta h = 60 \mu\text{m}$, green laser, hatch = $120 \mu\text{m}$). Influence of scan speed

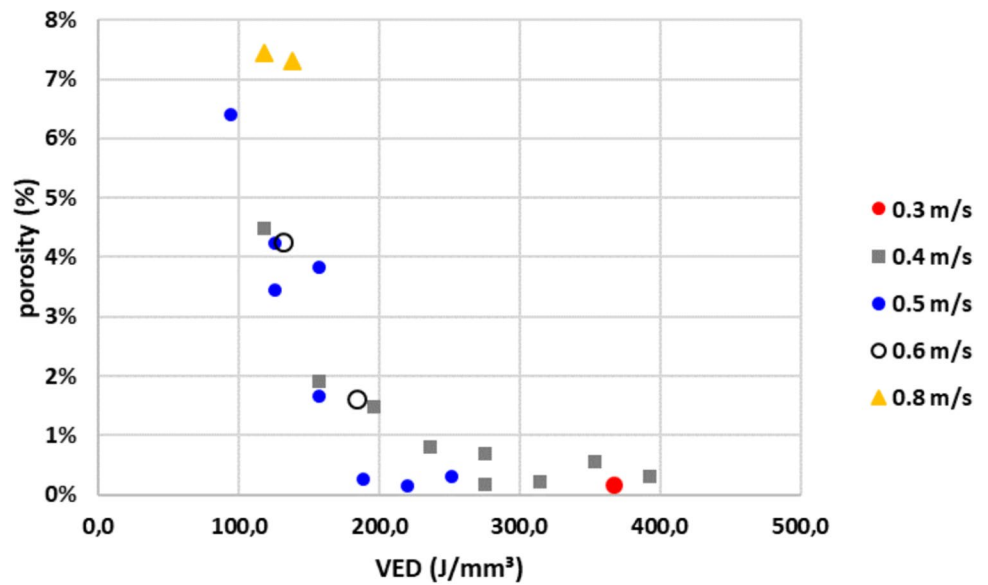


Fig. 13 Porosity vs VED ($\Delta h = 100 \mu\text{m}$, $150 \mu\text{m}$, variable hatch distances, scan speed comprised between 0.4 and $0.8 \text{ m}\cdot\text{s}^{-1}$, $\lambda = 515 \text{ nm}$)

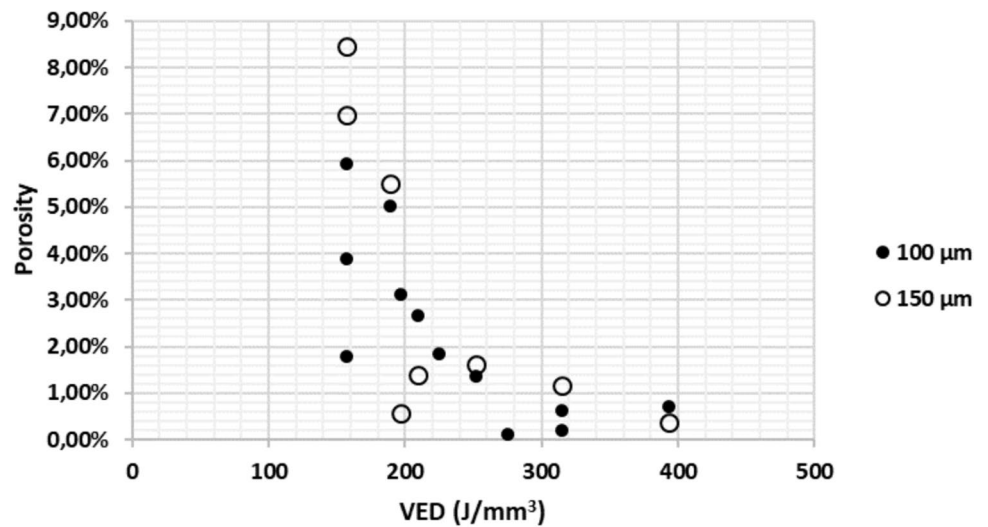
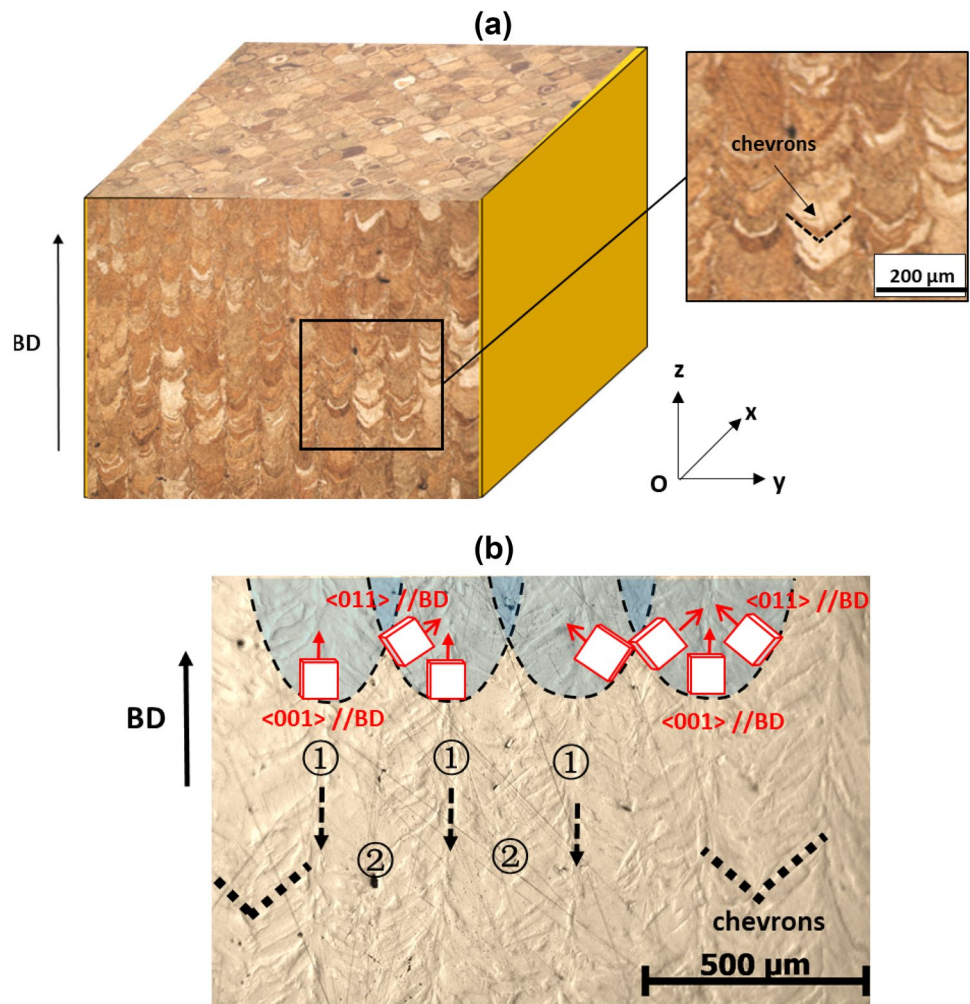


Fig. 14 Microstructural analysis of pure copper manufactured by a green LPBF (optical microscopy) with $P=0.6$ kW, $V=0.5$ m/s, Hatch = 150 μm , **a** with chemical etching, **b** $P=0.6$ m/s, $V=0.5$ m/s, Hatch = 300 μm – $\Delta h=150$ μm (G-36 sample), without chemical etching (OPS polishing), FCC crystal orientations are indicated in red



Inverse pole figures (IPF) EBSD maps confirm this columnar microstructure oriented parallel to BD on a cross-sectional view (Fig. 15b) and also confirm the regular pavement on (O, x, y) planes (Fig. 15a). They also indicate a $\langle 011 \rangle$ crystal orientation//BD, with a texture index of about ~ 15 .

Such a chevron-like columnar microstructure and $\langle 011 \rangle$ texture indicate a 0° or 90° rotation angle between subsequent layers combined with a keyhole welding regime already analyzed in detail by Andreau et al. [24]. For such conditions, the solidification front is not perpendicular to the build direction, but approximately tilted with a 45° angle vs BD. Therefore, the resulting microstructure is controlled by the local inclination ($+45^\circ$ and -45°) of each melt-pool lateral edge vs BD, combined with side branching effects of solidification cells inside grains between adjacent melt pools [25].

As investigated in detail by Sofinowski et al. [25] on 316L, such microstructures can easily be tuned along (O, x) or (O, y) by a modification of scan angle, with preservation of $\langle 011 \rangle$ //BD texture, if no scan angle was used between

subsequent layers. One major difference between pure copper and other alloys is the absence of segregation that prevents a precise detection of solidification cells on microstructures.

Local FCC lattice orientations (Fig. 15a and b) show that the $\langle 011 \rangle$ //BD crystal orientation is maintained all along the build. However, when considering crystal orientation along scan directions (O, X) or (O, y), 90° tilts vs (O, z) are observed between adjacent scan lines (Fig. 15a).

Comparatively, copper samples manufactured with the E-PBF technique, which correspond to wider and less penetrated beads, exhibit a clear (001) texture, with a solidification front perpendicular to the BD, as shown by Thomas et al. [11]. From these results, it can be assumed that due to the high conductivity of pure copper, LPBF with an 80–100- μm laser beam necessitates a high-energy/deep penetration regime which systematically promotes a $\langle 110 \rangle$ texture instead of a $\langle 001 \rangle$, more usual on additively manufactured fcc metals.

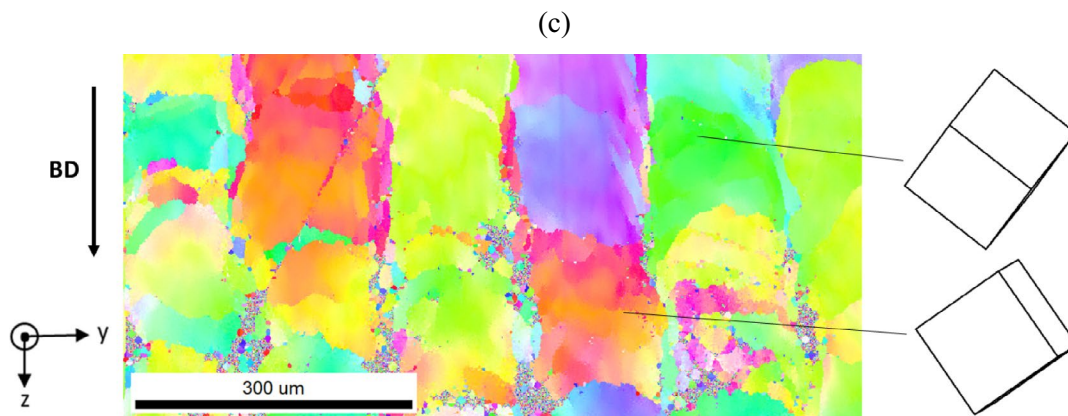
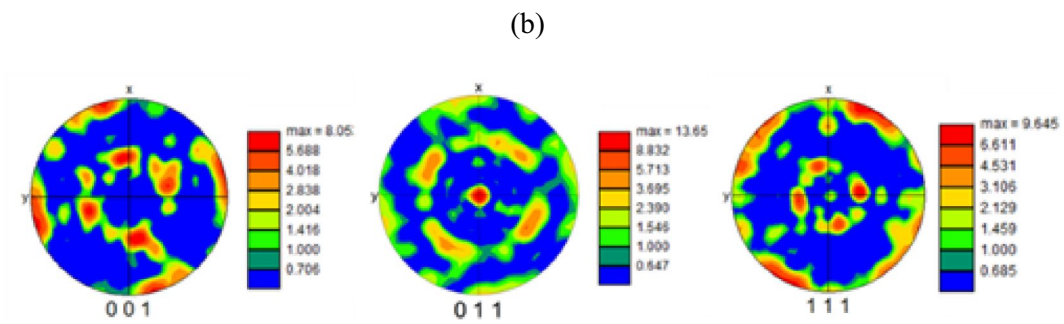
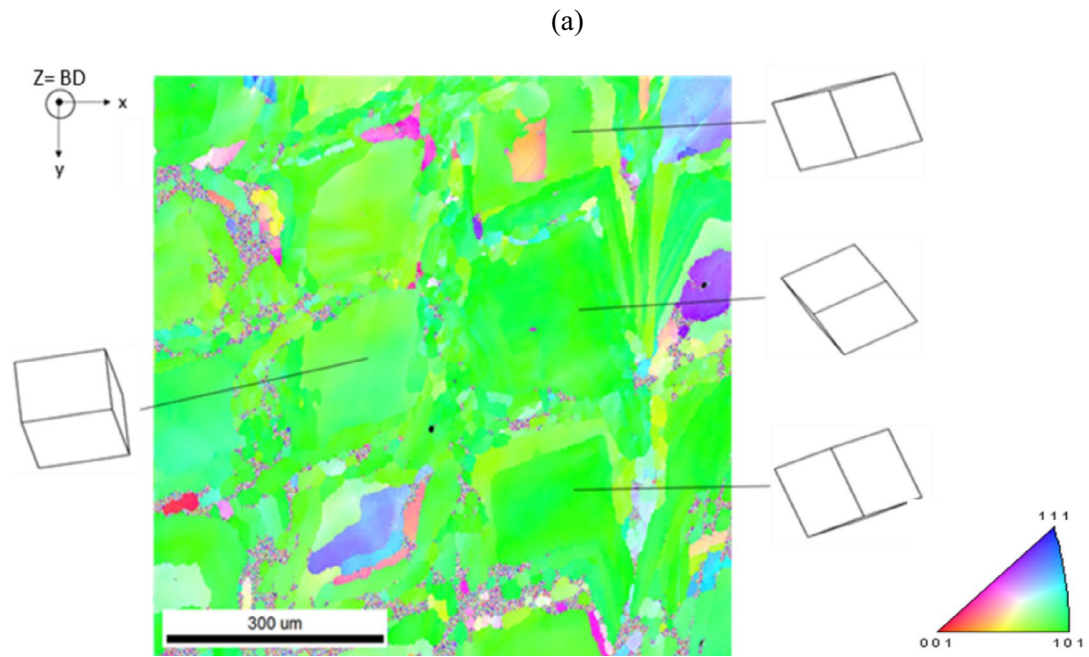


Fig. 15 Inverse pole figures (IPF-EBSD) (a) and pole figures (PF) (b) of pure copper built with a green laser wavelength on (O, x, y)=build surface, c IPF on (O, y, z)=cross-section. IPF color codes for all

maps are represented with the z-axis parallel to the building direction ($P=600$ W, $V=0.5$ m/s, hatch= $200\ \mu\text{m}$)

4.4 Hardness and dislocation density of as-built and heat-treated copper samples

LPBF samples usually exhibit, whatever the material, a high dislocation density, due to a fast melt pool shrinkage during solidification. This results in thermal-induced hardening, with a magnitude comparable to a 10–15% plastic deformation. This phenomenon is specific to materials produced through laser powder bed fusion (LPBF) but has only been previously studied in alloyed metals [26].

On pure LPBF copper, the only contributions to hardening-strengthening are grain boundaries (Hall–Petch-like) and dislocations. The other usual contributions (solid solution strengthening, precipitation hardening) can be neglected on a pure metal.

Analytically, the Hall–Petch contribution on polycrystalline copper follows a $\sigma = \sigma_0 + k.d^{-0.5}$ contribution, with $\sigma_0 = 20$ MPa and $k = 0.16$ MPa $m^{0.5}$ for 10–150 μm grains [27] whereas the dislocation forest strengthening is defined by Eq. (3), with $\alpha =$ geometric constant, $M =$ Taylor’s factor, $b =$ burgers vector, $G =$ Shear modulus, $\rho_d =$ dislocation density.

$$\Delta\sigma_{dis} = \alpha MbG\rho_d^{1/2} \quad (3)$$

The estimation of work-hardening is mostly possible using various methods such as (1) hardness tests, (2) the analysis of Kernel Average Misorientation maps from EBSD data, (and 3) the analysis of X-ray peak broadening. All three methods were tested in the current work, before and after heat treatment (1 h/200 °C and 1 h/500 °C). Such heat treatments are usually sufficient to provide softening and stress relief on mechanically work-hardened copper [28]. Here, these two heat treatments did not modify distinctly grain size distributions of LPBF copper but have been used as an attempt to reduce dislocation density.

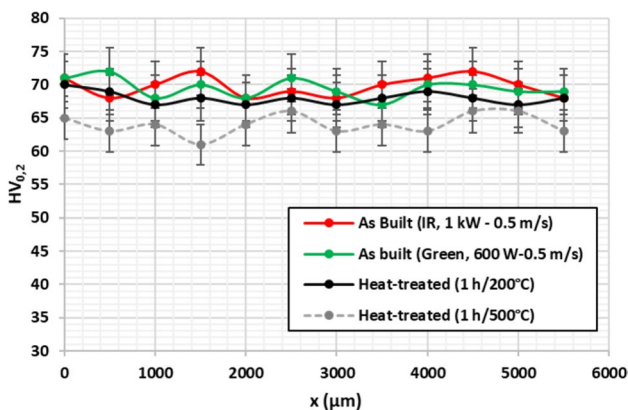


Fig. 16 Micro-hardness tests (0.2 fkg) on as-built and heat-treated samples

Hardness measurements were first carried out on as-built samples (with both green and IR wavelengths) and heat-treated samples, for LPBF conditions allowing an optimum densification. Initially, no discernible difference was noted between samples produced using a 1 Kw–0.5 m/s (infrared) and a 600 W–0.5 m/s (green) setup. This confirms that, despite a nearly identical absorbed power, there is no observable distinction between infrared and green wavelengths. An average value of 70 $HV_{0.2}$ was obtained on as-built samples, which is 40% higher than the hardness of pure copper obtained with E-BPF (around 50 $HV_{0.5}$ in [11]). Second, heat treatments induced a moderate thermal softening: 68 $HV_{0.2}$ for 200 °C, 1 h and 64 $HV_{0.2}$ for 1 h/500 °C (Fig. 16).

Fast analysis of the KAM EBSD profiles confirmed that, like most of the LPBF materials, a high density of geometrically necessary dislocations (GND) is shown (average estimated value between 10^{15} and 10^{16} $m.m^{-3}$), due to the high solidification rate of tiny LPBF melt pools. Geometrical necessary dislocations (GND) represent the number of dislocations required to achieve a similar degree of crystal misorientation locally, typically between adjacent pixels on electron backscatter diffraction (EBSD) maps. They mostly provide a quantitative estimation of the work-hardening at the polycrystalline material scale.

This confirms afterward that on LPBF-built alloys, segregation effects, usually coincident with high dislocation densities [29], do not play a dominant role in dislocation generation, while similar GND densities are shown on a pure metal like copper. Moreover, no clear modification of IPF and KAM profiles was detected following 200 °C and 500 °C heat treatments, confirming no recrystallization has started and that stress relief was not fully effective at 1 h/500 °C.

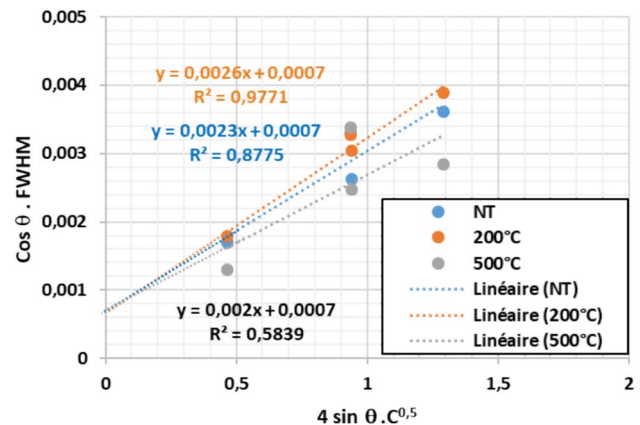


Fig. 17 Williamson–Hall analytical method applied to X-ray data (Eq. 2). With the use of the C parameter as a phase contrast of dislocations on diffracting planes, satisfactory regression coefficients were obtained, which allowed an estimation of dislocation density

Additional investigations were carried out considering X-ray peak broadening and using the Williamson–Hall analytical approach [30] modified by Ungar [31] considering the phase contrast of dislocations of fcc pure copper for the different (hkl) planes ($C_{111} = 0.099$, $C_{200} = 0.304$, $C_{220} = 0.150$, and $C_{311} = 0.207$). Such an approach identifies both the influence of crystallite size and dislocations in the X-ray peak broadening and has been tested successfully by Prasad et al. [32] on an IN718 alloy built with LPBF.

From the slopes of (FWHM. $\cos\theta$) vs ($4\sin(\theta \cdot C)^{0.5}$) curves (Fig. 17), distortions $\dot{\epsilon}$ of the crystal were determined and allowed estimating the dislocation density ρ_d with Eq. (5). Obtained values were as follows: $\rho_d = 1.4 \cdot 10^{15} \text{ m}^{-2}$ (as-built), $\rho_d = 1.6 \cdot 10^{15} \text{ m}^{-2}$ (heat-treated 200 °C), $\rho_d = 0.9 \cdot 10^{15} \text{ m}^{-2}$ (heat-treated 500 °C). Such elevated ρ_d values confirm that as-built copper is hardened by the dislocations, but indicate that heat treatments did not provide a significant tempering of the specimens.

$$\text{FWHM}\cos(\theta_{\text{hkl}}) = 4\sin(\theta_{\text{hkl}}) \cdot C^{0.5} \cdot \dot{\epsilon} + \frac{0.9\lambda_X}{D_S}, \quad (4)$$

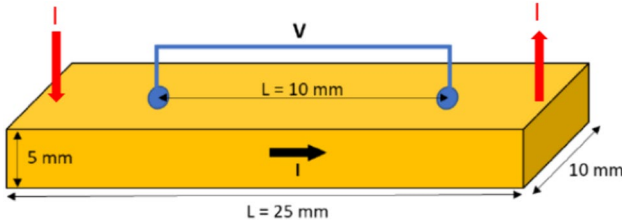


Fig. 18 Electrical measurements with the 4-probe device

where FWHM = full width at half maximum of X-ray peaks ($^\circ$), θ = Bragg angle ($^\circ$), λ_x = wavelength of anticathode (m), D_s = size of diffracting crystallites (m), C = phase contrasts of dislocations on (hkl) planes

$$\rho_d = \frac{16.1\dot{\epsilon}}{b^2}, \quad (5)$$

where b = Burgers vector (m).

5 Electrical properties of LPBF samples built with a green laser source

Many factors can influence the electrical properties of polycrystalline metals.

Electrical properties were estimated at Schneider Electric on a selection of 25 mm \times 10 mm \times 5 mm parallelepiped samples built with the green laser. Tests were carried out using a classical 4-probe device (Fig. 18), where a continuous I current is applied between two probes and the voltage is recorded between two other probes separated by a distance L of 10 mm [11].

One can then deduce the electrical resistance R of the specimen and the electrical conductivity σ_{el} using Eq. (6) here below.

$$R = \frac{U}{I} \quad \text{and} \quad \sigma_{el} = \frac{1}{R} \cdot \frac{L}{S}, \quad (6)$$

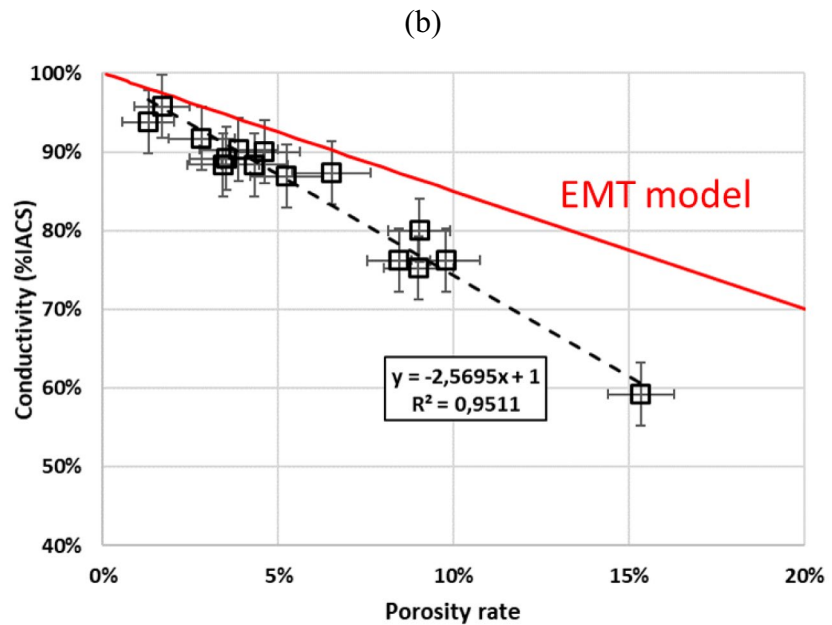
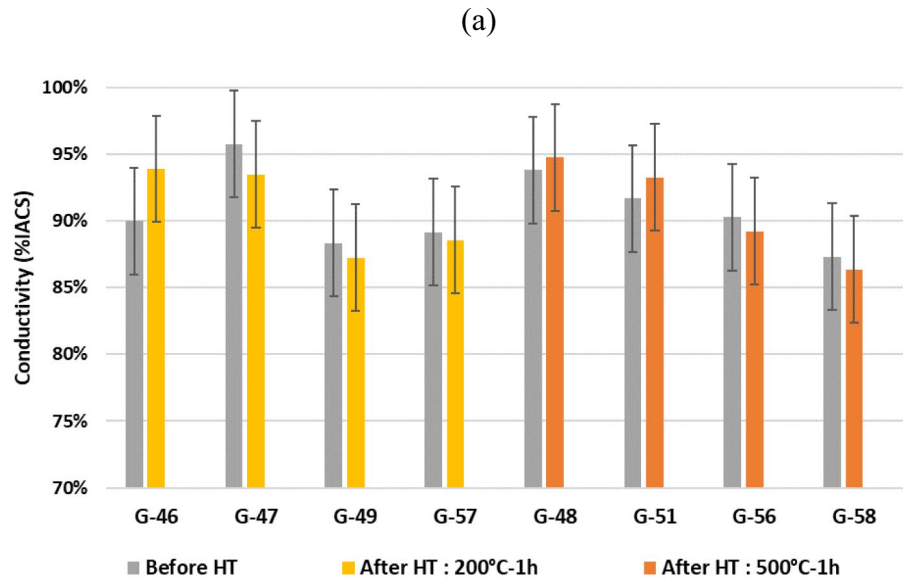
where σ_{el} = electrical conductivity ($\text{S} \cdot \text{m}^{-1}$), R = resistance (ohm), U = voltage (V), I = applied current (A), L = inter-probe distance (= 10 mm), S = section (= $5 \times 10 = 50 \text{ mm}^2$).

Contrary to previous porosity rate measurements with image analysis on cross-sections, the porosity rate has been

Table 5 Electrical conductivity of LPBF samples ($\Delta h = 60 \mu\text{m}$) before and after heat treatment (*200 °C, 1 h or **500 °C, 1 h)

Name	Hatch H (μm)	P (W)	V (m/s)	VED (J/mm^3)	Porosity rate	σ_{el} (% IACS)	σ_{el} (HT) (% IACS)
G-44	200	300	0.5	94	15%	59%	
G-45	200	400	0.5	126	8.5%	75%	
G-46	200	500	0.5	157	2%	90%	94%*
G-47	200	600	0.5	189	1%	96%	93%*
G-48	200	700	0.5	220	0.5%	93.7%	94.6%**
G-49	200	600	0.7	135	3.0%	88%	87%*
G-50	150	1000	0.8	197	9%	92%	
G-51	300	1000	0.5	314	2.5%	91.5%	93%**
G-52	150	400	0.4	157	8%	76%	
G-53	150	500	0.5	157	4%	88%	
G-54	150	400	0.8	79	9.5%	87%	
G-55	150	500	0.8	98	5%	90%	
G-56	150	600	0.8	118	3%	86.5%	87.2%**
G-57	150	700	0.8	138	3%	88.5%	88%*
G-58	150	1000	1.5	105	6%	87%	86%**

Fig. 19 a Electrical conductivity of LPBF samples before and after heat treatment, **b** electrical conductivity of LPBF samples vs porosity rate ($\Delta h = 60 \mu\text{m}$) and comparison with EMT model. A linear regression, in a dotted line, on experimental data is also indicatively added to the graph



determined by the measurement of the mass of the sample and the real dimensions (and volume) of each sample. The precision of the porosity rate measures is $\pm 1\%$ due to the accuracy of the volumetric measurement. In addition, some of the tested samples have also been heat treated—1 h at 200 °C and 1 h at 500 °C—to provide stress relief and a reduction of dislocation density, possibly impacting electrical conductivity (Table 5).

Maximum electrical conductivity of 96% IACS was obtained on as-built copper for the larger densities obtained in the working campaign (around 0.5–1%), with a rather limited effect of heat treatment (Fig. 19a). However, no

clear evolution of the GND density was shown after HT, which seems to indicate a stable dislocation network, and that a longer or a higher time maintain HT would be necessary to promote a real tempering effect, with possible recrystallization phenomena.

For the large range of porosity rates (between 0.5 and 15%), a quasi-linear reduction of electrical conductivity was shown (Fig. 19b), which would demand numerous data to be confirmed. To provide a deeper understanding of this linear correlation, several analytical models of thermal conductivity for multi-phase materials were used, assuming a direct correlation between electrical and

thermal conductivities thanks to Wiedemann–Franz law: $K = LT\sigma$ (with K = electrons-driven thermal conductivity, σ = electrical conductivity, L = Lorentz number, T = temperature). In such models, the pores were considered a second phase with the Argon thermal conductivity ($0.017 \text{ W.K}^{-1}.\text{m}^{-1}$). Finally, a relatively correct fitting with experiments was obtained using an effective medium theory (EMT) model [33] of thermal conductivity for heterogeneous materials (Eq. 5).

$$K_{eq} = \frac{2(1 - \varepsilon)K_s^2 + (1 + 2\varepsilon)K_sK_f}{(2 + \varepsilon)K_s + (1 - \varepsilon)K_f}, \quad (7)$$

where K_{eq} = equivalent conductivity, K_s = solid conductivity ($390 \text{ W.m}^{-1}.\text{K}^{-1}$ for copper), K_f = fluid (Argon) conductivity ($0.017 \text{ W.m}^{-1}.\text{K}^{-1}$), ε = porosity.

6 Discussion

In the current paper, the ability of both IR and green 1 kW lasers to build more than 99.5% dense pure copper with LPBF was demonstrated, which corresponds to a step forward compared with preliminary works [4–6] using non-coated copper powder.

With the 1 kW laser, the first set of experiments was hindered by the thermal instability of the scan head and focusing optics at elevated power. Such a phenomenon induced an instantaneous beam defocusing which limited densification, except for the smallest parts (Fig. 5a). A second step of experiments using inter-track time pauses to limit excessive heating of the optics and short fusion vectors allowed obtaining up to 99.8% densification and fusion rates close to $20 \text{ cm}^3/\text{h}$. Similar densities were obtained with a thermally stable scan head at the AddUp facility.

For all the IR tests, an input power of at least 800 W and a maximum scan speed of 500 mm.s^{-1} were shown to be necessary to provide satisfactory densification. This densification occurred for energy densities (VED) superior to 200 J/mm^3 (Fig. 12). This result seems coherent with other literature data on pure LPBF copper [6, 8], but not with the work by Yan et al. [7] who considered much lower IR laser powers ($< 200 \text{ W}$).

The remaining pores observed for the optimized IR process conditions (Fig. 8) are believed to be keyhole pores, especially because a keyhole mode was shown to be mandatory to obtain continuous beads and correct densification in IR with a $70 \mu\text{m}$ spot diameter and a $50 \mu\text{m}$ layer thickness. Consequently, such porosities consistently manifest, albeit to a minor degree, in rather dense copper parts when an IR wavelength is utilized.

With a 1 kW green laser, up to 99.9% densification was demonstrated, for a two times lower output power ($\sim 450\text{--}500 \text{ W}$) than in IR, due to the two times lower absorptance of liquid copper at $0.515 \mu\text{m}$ [17]. However, higher laser powers did not allow using higher scan speeds to reach equivalent densification, and the optimum scan speeds were always below 0.6 m/s . Above 500 W and 600 mm.s^{-1} , fused copper was shown to be more unstable, with more spatters and larger ones compared to usual LPBF materials, and prevented optimum densification. This could be explained by the combination of low surface tension ($\gamma = 1.2 \text{ N/m}$) compared with usual metals such as Ti, Fe, or Ni alloys ($\gamma = 1.5\text{--}1.8 \text{ N/m}$) [22], and elevated VED values.

The main observed difference between IR and green LPBF is that, at $\lambda = 1.08 \mu\text{m}$, due to the high reflectivity of the solid substrate and melt pools, better process stability and laser–matter coupling are mostly obtained when positioning the laser tracks on the powder bed, i.e., with high hatch distances allowing to avoid laser irradiation on denuded areas. Comparatively, a green laser LPBF is more tolerant concerning laser positioning, and scan strategy. Green LPBF allows obtaining higher fusion rates ($\sim 64 \text{ cm}^3/\text{h}$) combined with the use of large hatch distances ($300 \mu\text{m}$) and deeper powder layer ($150 \mu\text{m}$), for two times lower laser power ($\sim 500 \text{ W}$). Such fusion rates are much higher than in previously published works [6]. However, the melt pool stabilization evidenced by previous works with a green laser in a “deep” penetration ($> 1 \text{ mm}$) welding regime [15, 16] at lower power densities is not evidenced in the current work.

For laser diameters of $60\text{--}90 \mu\text{m}$, whatever the wavelength, the high density was systematically obtained with a deep keyhole welding mode allowing stable fusion tracks. This resulted in a chevron microstructure and a $\langle 011 \rangle$ texture parallel to the build direction, contrary to previous E-PBF works indicating a strong $\langle 001 \rangle$ crystallographic texture [11]. This LPBF texture is directly due to the 45° inclination of the melt pool edges vs BD.

A specific focus was put on dislocation density analysis using X-ray diffraction before and after 200°C and 500°C heat treatment. High ($\sim 10^{15} \text{ m}^{-2}$) and stable dislocation densities were shown. As copper is a pure metal, this confirms that segregation effects do not play any specific role in dislocation formation. In future works, the origin and the stability of dislocation density [29] vs thermal treatment, and the recrystallization kinetics of LPBF pure copper should constitute an interesting oncoming research task to address.

Satisfactory but lower-than-expected electrical conductivities (up to 96% IACS) were obtained on as-built and heat-treated LPBF copper, with powers of at least 800

W in IR and 600 W in green. As indicated in Ref. [12], pure copper is a highly conductive material, due to the occurrence of a unique electron in its last electronic orbital. However, various factors can decrease its electrical conductivity σ_c : porosity, impurity atoms (O, N, P), grain boundaries (especially for grains below 1 μm), and dislocations.

In the current work, the rather low σ_c obtained (max 96% IACS) could partly be due to the stable and high dislocation density generated by the process, to a small oxygen contamination in the LPBF chamber, and more obviously to the remaining pore density ($\sim 0.5\%$). However, such an explanation should be confirmed by additional measurements.

Spreading powder bed layers thinner than 60 μm could also serve as a compelling approach to facilitate using lower laser powers while constraining the keyhole welding mode (Fig. 9).

Finally, using pure copper in heat exchangers or electrical connectors requires a good compromise between thermal–electrical conductivity and mechanical strength.

Therefore, in future works, it would be interesting to focus on the mechanical resistance of pure copper parts obtained with high power densities/volume energy densities. The mechanical strength of LPBF materials is a key point for nearly all LPBF alloys (titanium alloys, stainless steels, etc.), but little to no study on pure materials [34].

As a preliminary insight, the pure LPBF copper obtained in the current work can be compared with Yan et al. work [6] which achieved 99% dense material. The corresponding hardness was between 70 and 80 HV (70 HV in our case: Fig. 16), and the tensile strengths were in the 220–240 MPa range, with rather low elongations ($A\% < 15$). We can suppose that our built samples should exhibit nearly similar tensile strength data, which meets the minimum requirement of wrought parts.

Oncoming works on (Ni, C)-coated copper powders [35] should also provide additional insight into the manufacturability of pure copper with IR wavelength.

7 Conclusion

In summary, the present original work compares 1 kW IR and green laser powder bed fusion on pure copper.

First, a process optimization was carried out on single LPBF tracks to estimate stability domains, with optimized output powers above 800 W in IR and above 400 W at 515 nm. Second, from these optimized parameters, more than 99.5% dense LPBF pure copper was obtained on 3D parts using either IR or green wavelength 1 kW lasers. In terms of process efficiency, the main difference observed between IR and green LPBF was the ability to use a two times lower laser power with a green wavelength, due to the

two times higher absorptance of liquid copper at 515 nm, and the possibility to obtain higher fusion rates with thicker powder layers.

Third, similar microstructures were obtained with the two laser irradiations, with a $\langle 011 \rangle$ //BD crystal predominant texture and high estimated dislocation densities near 10^{15} m^{-2} .

Last, a maximum of 96% IACS conductivity was measured on as-built and heat-treated LPBF copper samples, and confronted with analytical electrical conductivity models.

Finally, this work provides a useful and novel insight into the build ability of pure copper with the LPBF process.

Acknowledgements The authors wish to thank AddUp and French ANRT for financial grant of the CIFRE PhD position. This work was carried out as part of the Ambition FUI project funded by BPI, Auvergne-Rhône-Alpes and Ile-de-France regions.

Author contributions All authors contributed to the study's conception and design. Material preparation, data collection, and analysis were performed by G. Nordet, P. Peyre F. Coste, P. Lapouge. The first draft of the manuscript was written by G. Nordet and all authors commented on previous versions of the manuscript. All authors read and approved the final manuscript.

Data availability Data are all in the article. Questions about data are available from the corresponding author on reasonable request.

Declarations

Conflict of interest The authors have no relevant financial or non-financial interests to disclose.

References

1. Bidare P (2018) Laser powder bed fusion in high-pressure atmospheres. *Int J Adv Manuf Technol* 99:543–555
2. Zhao C, Fezzaa K, Cunningham RW et al (2017) Real-time monitoring of laser powder bed fusion process using high-speed X-ray imaging and diffraction. *Sci Rep* 7:3602. <https://doi.org/10.1038/s41598-017-03761-2>
3. Nasuta DM, Halota A, Zhao A, Mzhen M (2022) Advanced copper heat exchangers from low-cost additive manufacturing techniques. *Int Air Conditioning Conference*. <https://docs.lib.purdue.edu/iracc/2310>
4. Jadhav SD, Dadbakhsh S, Goossens L et al (2019) Influence of selective laser melting process parameters on texture evolution in pure copper. *J Mater Process Technol* 270:47–58. <https://doi.org/10.1016/j.jmatprotec.2019.02.022>
5. Jadhav SD, Goossens LR, Kinds Y et al (2021) Laser-based powder bed fusion additive manufacturing of pure copper. *Addit Manuf* 42:101990. <https://doi.org/10.1016/j.addma.2021.101990>
6. Colopi M, Demir AG, Caprio L, Previtali B (2019) Limits and solutions in processing pure Cu via selective laser melting using a high-power single-mode fiber laser. *Int J Adv Manuf Technol* 104:2473–2486. <https://doi.org/10.1007/s00170-019-04015-3>
7. Yan X, Chang C, Dong D et al (2020) Microstructure and mechanical properties of pure copper manufactured by selective

- laser melting. *Mater Sci Eng A* 789:139615. <https://doi.org/10.1016/j.msea.2020.139615>
8. Jadhav SD, Vleugels J, Kruth J et al (2020) Mechanical and electrical properties of selective laser-melted parts produced from surface-oxidized copper powder. *Mater Des Process Commun*. <https://doi.org/10.1002/mdp2.94>
 9. Jadhav S, Dadbakhsh S, Vleugels J et al (2019) Influence of carbon nanoparticle addition (and impurities) on selective laser melting of pure copper. *Materials* 12:2469. <https://doi.org/10.3390/ma12152469>
 10. Lindström V, Liashenko O, Zwiackner K et al (2020) Laser powder bed fusion of metal coated copper powders. *Materials* 13:3493. <https://doi.org/10.3390/ma13163493>
 11. Thomas A (2021) Processing of pure copper by Electron Powder Bed Fusion (E-PBF)
 12. Jadhav SD, Fu D, Deprez M et al (2020) Highly conductive and strong CuSn0.3 alloy processed via laser powder bed fusion starting from a tin-coated copper powder. *Addit Manuf* 36:101607. <https://doi.org/10.1016/j.addma.2020.101607>
 13. Hu D, Lu R, Huang Y et al (2020) Effects of optical variables in a single integrating sphere system on estimation of scattering properties of turbid media. *Biosyst Eng* 194:82–98. <https://doi.org/10.1016/j.biosystemseng.2020.03.012>
 14. Engler S, Ramsayer R, Poprawe R (2011) Process studies on laser welding of copper with brilliant green and infrared lasers. *Phys Procedia* 12:339–346. <https://doi.org/10.1016/j.phpro.2011.03.142>
 15. Chung W-S, Olowinsky A, Gillner A (2020) Process studies on copper laser beam welding over gap by using disc laser at green wavelength. *J Adv Join Process* 1:100009. <https://doi.org/10.1016/j.jajp.2020.100009>
 16. Punzel E, Hugger F, Dörringer R et al (2020) Comparison of different system technologies for continuous-wave laser beam welding of copper. *Procedia CIRP* 94:587–591. <https://doi.org/10.1016/j.procir.2020.09.081>
 17. Nordet G, Gorny C, Mayi Y et al (2022) Absorptivity measurements during laser powder bed fusion of pure copper with a 1 kW cw green laser. *Opt Laser Technol* 147:107612. <https://doi.org/10.1016/j.optlastec.2021.107612>
 18. Kohl S, Kaufmann F, Schmidt M (2022) Why color matters—proposing a quantitative stability criterion for laser beam processing of metals based on their fundamental optical properties. *Metals* 12:1118. <https://doi.org/10.3390/met12071118>
 19. Hummel M, Schöler C, Häusler A et al (2020) New approaches on laser micro welding of copper by using a laser beam source with a wavelength of 450 nm. *J Adv Join Process* 1:100012. <https://doi.org/10.1016/j.jajp.2020.100012>
 20. Sow MC, De Terris T, Castelnaud O et al (2020) Influence of beam diameter on laser powder bed fusion (L-PBF) process. *Addit Manuf* 36:101532. <https://doi.org/10.1016/j.addma.2020.101532>
 21. Kaiser E, Dold E-M, Killi A, Zaske S. Application benefits of welding copper with a 1 kW, 515 nm continuous wave laser. 6
 22. Mills KC (2002) Recommended values of thermophysical properties for selected commercial alloys. Woodhead, Cambridge
 23. Fabbro R (2019) Scaling laws for the laser welding process in keyhole mode. *J Mater Process Technol* 264:346–351. <https://doi.org/10.1016/j.jmatprotec.2018.09.027>
 24. Andreau O, Koutiri I, Peyre P et al (2019) Texture control of 316L parts by modulation of the melt pool morphology in selective laser melting. *J Mater Process Technol* 264:21–31. <https://doi.org/10.1016/j.jmatprotec.2018.08.049>
 25. Sofinowski KA, Raman S, Wang X et al (2021) Layer-wise engineering of grain orientation (LEGO) in laser powder bed fusion of stainless steel 316L. *Addit Manuf* 38:101809. <https://doi.org/10.1016/j.addma.2020.101809>
 26. De Terris T, Castelnaud O, Hadjem-Hamouche Z et al (2021) Analysis of as-built microstructures and recrystallization phenomena on Inconel 625 alloy obtained via laser powder bed fusion (L-PBF). *Metals* 11:619. <https://doi.org/10.3390/met11040619>
 27. Chen F, Wang Q, Zhang C et al (2022) Microstructures and mechanical behaviors of additive manufactured Inconel 625 alloys via selective laser melting and laser engineered net shaping. *J Alloys Compd* 917:165572. <https://doi.org/10.1016/j.jallcom.2022.165572>
 28. Barbery J (1991) Traitements thermiques du cuivre et de ses alliages, 23
 29. Bertsch KM, Meric de Bellefont G, Kuehl B, Thoma DJ (2020) Origin of dislocation structures in an additively manufactured austenitic stainless steel 316L. *Acta Mater* 199:19–33. <https://doi.org/10.1016/j.actamat.2020.07.063>
 30. Williamson GK, Hall WH (1953) X-ray line broadening from filed aluminium and wolfram. *Acta Metall* 1:22–31. [https://doi.org/10.1016/0001-6160\(53\)90006-6](https://doi.org/10.1016/0001-6160(53)90006-6)
 31. Ungár T (1998) Strain broadening caused by dislocations. *Mater Sci Forum* 278–281:151–157. <https://doi.org/10.4028/www.scientific.net/MSF.278-281.151>
 32. Prasad K, Obana M, Ito A, Torizuka S (2021) Synchrotron diffraction characterization of dislocation density in additively manufactured IN 718 superalloy. *Mater Charact* 179:111379. <https://doi.org/10.1016/j.matchar.2021.111379>
 33. Wang J, Carson JK, North MF, Cleland DJ (2008) A new structural model of effective thermal conductivity for heterogeneous materials with co-continuous phases. *Int J Heat Mass Transf* 51:2389–2397. <https://doi.org/10.1016/j.ijheatmasstransfer.2007.08.028>
 34. Khosravani MR, Reinicke T (2021) Fracture behavior of intact and defected 3D-printed parts. *Procedia Struct Integr* 31:105–110. <https://doi.org/10.1016/j.prostr.2021.03.017>
 35. Crespi AE, Nordet G, Peyre P et al (2023) The use of sacrificial graphite-like coating to improve fusion efficiency of copper in selective laser melting. *Materials* 16:2460. <https://doi.org/10.3390/ma16062460>